

# Dynamic Coupling and Allosteric Networks in the $\alpha$ Subunit of Heterotrimeric G Proteins<sup>\*[5]</sup>

Received for publication, November 12, 2015, and in revised form, December 14, 2015. Published, JBC Papers in Press, December 24, 2015, DOI 10.1074/jbc.M115.702605

Xin-Qiu Yao<sup>†1</sup>, Rabia U. Malik<sup>§1</sup>, Nicholas W. Griggs<sup>||</sup>, Lars Skjærven<sup>\*\*</sup>, John R. Traynor<sup>||</sup>, Sivaraj Sivaramakrishnan<sup>¶</sup>, and Barry J. Grant<sup>‡2</sup>

From the Department of<sup>†</sup>Computational Medicine and Bioinformatics, <sup>§</sup>Cell and Developmental Biology, and <sup>||</sup>Pharmacology, University of Michigan, Ann Arbor, Michigan 48109, the <sup>\*\*</sup>Department of Biomedicine, University of Bergen, 5020 Bergen, Norway, and the <sup>¶</sup>Department of Genetics, Cell Biology, and Development, University of Minnesota, Minneapolis, Minnesota 55455

G protein  $\alpha$  subunits cycle between active and inactive conformations to regulate a multitude of intracellular signaling cascades. Important structural transitions occurring during this cycle have been characterized from extensive crystallographic studies. However, the link between observed conformations and the allosteric regulation of binding events at distal sites critical for signaling through G proteins remain unclear. Here we describe molecular dynamics simulations, bioinformatics analysis, and experimental mutagenesis that identifies residues involved in mediating the allosteric coupling of receptor, nucleotide, and helical domain interfaces of  $G\alpha_i$ . Most notably, we predict and characterize novel allosteric decoupling mutants, which display enhanced helical domain opening, increased rates of nucleotide exchange, and constitutive activity in the absence of receptor activation. Collectively, our results provide a framework for explaining how binding events and mutations can alter internal dynamic couplings critical for G protein function.

Heterotrimeric G proteins are key mediators of intracellular signaling pathways that control diverse cellular processes ranging from movement and division to differentiation and neuronal activity (1). G proteins consist of three subunits:  $G\alpha$ ,  $G\beta$ , and  $G\gamma$ . Bound with GDP,  $G\alpha$  forms an inactive complex with its  $G\beta\gamma$  subunit partners. Interaction with activated receptor (GPCR)<sup>3</sup> promotes the exchange of GDP for GTP on  $G\alpha$  and its separation from  $G\beta\gamma$ . Both isolated  $G\alpha$  and  $G\beta\gamma$  can then bind and activate or inhibit downstream effectors. GTP hydrolysis deactivates  $G\alpha$ , which subsequently reassociates with  $G\beta\gamma$  completing the cycle. This cycle is further regulated by two classes of additional proteins called regulators of G protein sig-

naling. These function as either GTPase-activating proteins (which promote GTP hydrolysis) or GDP dissociation inhibitors (GDIs, which hinder exchange of GDP for GTP) (2). Important conformational transitions occurring at each stage of this regulated cycle have been characterized from extensive crystallographic studies. These include GDP, GTP analogue,  $G\beta\gamma$ , GTPase-activating protein, GDI and most recently GPCR bound complex structures of  $G\alpha$ . However, the link between the observed conformations and the atomic level mechanisms involved in coupling receptor association, G protein activation, and effector interaction remain unclear.

All  $G\alpha$  proteins consist of a catalytic GTP binding Ras-like domain (termed RasD) and a heterotrimeric G protein specific helical domain (HD). Recent principal component analysis (PCA) of 53 available  $G\alpha$  crystallographic structures identified three major conformationally distinct groups (Fig. 1 and Ref. 3). These groups correspond to structures with bound GTP analogues, GDP, and GDI (*red*, *green*, and *blue* points in Fig. 1*a*, respectively). The major variation in the accumulated structures is the concerted displacements of three nucleotide-binding site loops termed the switch regions (SI, SII, and SIII), as well as a relatively small scale ( $<10^\circ$ ) rotation of the constituent HD and RasD regions. A much larger ( $127^\circ$ ) clam-shell like displacement of the HD with respect to RasD was reported recently in the crystallographic structure of *Gas* (the  $\alpha$  subunit of the stimulatory G protein for adenylyl cyclase) in complex with  $G\beta\gamma$  and the  $\beta_2$  adrenergic receptor (4). This conformational change, which effectively exposes the otherwise buried nucleotide binding site, has been linked to GPCR-mediated nucleotide exchange (4). Evidence for domain opening has also been obtained from recent electron microscopy (5), double electron-electron resonance analysis (6), hydrogen-deuterium exchange mass spectrometry (7), biochemical analysis (8), and molecular dynamics (MD) simulations (3, 9, 10). In addition, the structure of Rasmussen and co-workers (7) together with mass spectrometry results also confirm that both N-terminal  $\beta_1$  strand and C-terminal  $\alpha_5$  helix are major interaction sites for receptors. This supports the previously suggested role of these regions in coupling receptor binding and nucleotide dissociation activities (11–17). Despite these advances, critical questions remain unanswered: How do the distinct conformations evident in the accumulated structures interconvert? And critically, how do distal functional sites responsible for GPCR, nucleotide, and partner protein binding allosterically coordinate their activities? Addressing these questions requires infor-

\* This work was supported by University of Michigan, National Institutes of Health Grants R01-GM105646 (to S. S.) and R01-DA039997 (to J. R. T.), and American Heart Association Predoctoral Fellowship 14PRE18560010 (to R. U. M.). The authors declare that they have no conflicts of interest with the contents of this article. The content is solely the responsibility of the authors and does not necessarily represent the official views of the National Institutes of Health.

[5] This article contains supplemental Table S1 and S2.

<sup>1</sup> These authors contributed equally to this work.

<sup>2</sup> To whom correspondence may be addressed: 100 Washtenaw Ave., 2017 Palmer Commons Bldg., Ann Arbor, MI 48109-2218. Tel.: 734-647-3113; E-mail: bjgrant@umich.edu.

<sup>3</sup> The abbreviations used are: GPCR, G protein-coupled receptor; GDI, GDP dissociation inhibitor; RasD, Ras-like domain; HD, helical domain; PCA, principal component analysis; MD, molecular dynamics;  $A_1R$ , adenosine 1 receptor; Fsk, forskolin; PTX, pertussis toxin; GTP $\gamma$ S, guanosine 5'-3-O-(thio)triphosphate; PL, P-loop.

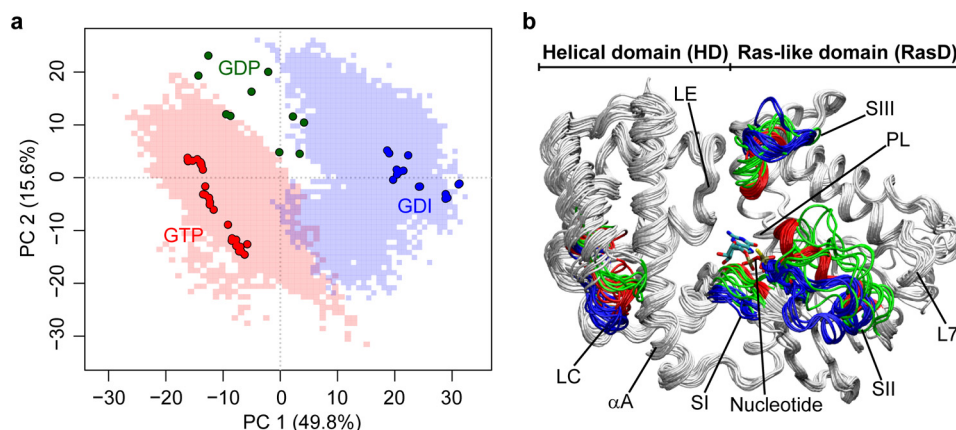


FIGURE 1. **Principal component analysis of crystallographic G $\alpha$  structures reveals three major conformations.** *a*, projection of 53 available Protein Data Bank crystal structures of G $\alpha$  (represented by round points; see also supplemental Table S1) onto the first two principal components (PC) that together account for 65.4% of the total structural variance. Three conformational clusters correspond to GTP-bound (red), GDP-bound (green), and GDI-bound (blue) structures. Projection of conformations sampled from MD simulations under GTP- and GDI-bound conditions are also shown as transparent red- and blue-shaded areas, respectively. *b*, superimposition of structures with high variance regions (SI, SII, SIII, and LC) colored by conformational cluster.

mation on protein dynamics, which is not directly available from the accumulated static experimental structures.

In this study, we aimed to dissect detailed mechanisms of allostery in G $\alpha$  by employing a combined computational and experimental approach. This entailed long time MD simulations, ensemble-based correlation network analysis of dynamic couplings related to allostery, and experimental mutagenesis and functional assays. This approach identified fluctuations and dynamic residue couplings in functional regions that distinguished GTP, GDP, and GDI states. Network analysis revealed a consistent bilobal dynamic partitioning of the RasD region. Partitioning of residues into these correlated segments was similar in different states but displayed distinct nucleotide dependent coupling strengths between segments. The active GTP state was shown to have the strongest overall couplings, exhibiting “dynamical tightening” with respect to GDP and GDI states. Furthermore, network path analysis delineated the detailed mechanism of dynamic coupling and revealed residues predicted to be involved in mediating the distal (>30 Å) allosteric coupling of receptor, nucleotide, and HD interfaces. Results from mutational simulations further supported the functional relevance of the identified allosteric paths with selected path mutations displaying a dynamic decoupling of distal sites along with an enhanced rate of spontaneous RasD-HD domain opening. Experimental mutagenesis of a number of these sites together with *in vitro* cAMP and [<sup>35</sup>S]GTP $\gamma$ S assays indicated that the signaling properties of G $\alpha_i$  can indeed be modulated by these single point mutations that act allosterically. In particular, the novel L32A mutation (numbering based on the  $\alpha$  subunit of bovine transducin) was predicted to enhance domain opening and was found to increase nucleotide exchange rates, increase G protein activation, and decouple G protein from receptor activation leading to constitutive activity.

## Experimental Procedures

All structure and trajectory analysis was performed with Bio3D version 2.0 (18, 19). Molecular graphics were generated with VMD version 1.9 (20).

*Crystallographic Structures Preparation*—Atomic coordinates for all crystallographic structures of the G $\alpha_i$  protein family were obtained from the RCSB Protein Data Bank (21) via sequence search utilities in the Bio3D package. Structures with unresolved residues in the switch regions were excluded from analysis leading to a data set containing 53 structural species (see supplemental Table S1 for full listing). Prior to assessing the variability of the structures, iterated rounds of structural superposition were performed to identify the most structurally invariant region. During this procedure, residues with the largest positional differences (measured as the volume of an ellipsoid determined from the Cartesian coordinates of the C $\alpha$  atoms) were removed, before each round of superposition, until only invariant core residues remained (22). The identified “core” structure was used as the reference frame for the superposition of crystal structures and subsequent MD trajectories prior to further analysis.

*Principal Component Analysis*—PCA was performed for the 53 crystallographic structures of G $\alpha$  to characterize interconformer relationship. The application of PCA to both distributions of experimental structures and MD trajectories, along with its ability to provide considerable insight into the nature of conformational differences in a range of protein families has been previously discussed (23–26). Briefly, PCA is based on the diagonalization of the variance-covariance matrix,  $\Sigma$ , with elements  $\Sigma_{ij}$  calculated from the Cartesian coordinates of C $\alpha$  atoms,  $r$ , after the superposition of all structures under analysis,

$$\Sigma_{ij} = \langle (r_i - \langle r_i \rangle) \cdot (r_j - \langle r_j \rangle) \rangle \quad (\text{Eq. 1})$$

where  $i$  and  $j$  enumerate all  $3N$  Cartesian coordinates. The eigenvectors, or principal components, of  $\Sigma$  form a linear basis set matching the distribution of structures. The variance of the distribution along each principal component is given by the corresponding eigenvalue. Projection of the distribution onto the subspace defined by principal components with the largest eigenvalues provides a low dimensional representation of structures facilitating analysis of interconformer relationships (Fig. 1*a*).

## Allostery in G Proteins

**Molecular Dynamics Simulations**—MD simulations were performed with AMBER12 (27) and corresponding force field ff99SB (28). Additional parameters for guanine nucleotides were taken from Meagher *et al.* (29). The  $Mg^{2+}$ ·GDP-bound transducin crystal structure (Protein Data Bank code 1TAG) was employed as the starting model for GDP-bound simulations. The  $Mg^{2+}$ ·GTP $\gamma$ S structure (Protein Data Bank code 1TND) was used as the starting model for GTP-bound simulations. The sulfur atom (S1 $\gamma$ ) in the GTP $\gamma$ S was replaced with the corresponding oxygen (O1 $\gamma$ ) of GTP. In addition, GDP-bound  $G\alpha_i$ /GoLoco motif complex structure (Protein Data Bank code 1KJY) was employed as the starting model for GDI-bound simulations. These structures were identified as cluster representatives from PCA. In all systems, Arg and Lys were protonated, whereas Asp and Glu were deprotonated. The protonation states for His residues were determined based on an inspection of the residues local environment and their  $pK_a$  values as calculated by PROPKA (30). Simulation structures were solvated in a truncated cubic box of pre-equilibrated TIP3P water molecules, which extended 12 Å in each dimension from the surface of the solute. Sodium counter ions ( $Na^+$ ) were added to neutralize the systems. Additional ions were not added to mimic physiological ionic strength. This may have the effect of accentuating electrostatic interactions. Energy minimization was performed in four stages, with each stage employing 500 steps of steepest descent followed by 1500 steps of conjugate gradient. First, minimization for solvent only was performed with fixed positions of protein and ligand atoms. Second, side chain and ligand were relaxed with backbone still fixed. Third, all protein and ligand atoms were relaxed with fixed solvent. Fourth, all atoms were free to move without any restraint. Following minimization, 10 ps of MD simulation was performed to heat the system from 0 to 300 K under constant volume periodic boundary conditions. A further 1 ns of equilibration simulation was performed at constant temperature ( $T = 300$  K) and constant pressure ( $p = 1$  bar). Subsequent 80-ns production phase MD was then performed under the same conditions as equilibration. For both energy minimization and MD simulations, the particle mesh Ewald summation method was adopted to treat long range electrostatic interactions. In addition, an 8 Å cutoff was used to truncate the short range nonbonded van der Waals' interactions. Additional operational parameters for MD included a 2-fs time step, removal of the center of mass motion every 1000 steps and update of the nonbonded neighbor list every 25 steps. All hydrogen atoms were constrained using the SHAKE algorithm.

**Correlation Network Construction**—Network analysis of correlated motions was employed to identify protein segments with coupled dynamics. A weighted network graph was constructed where each node represents an individual residue and the weight of the connection between nodes,  $i$  and  $j$ , represents their respective cross-correlation value,  $c_{ij}$  (31). This well established cross-correlation approach is based on linear atomic displacements during the course of simulations. Our evaluation of more recently developed nonlinear mutual information of dihedral angle changes (32, 33) indicated that prohibitively longer simulation and analysis time were likely required for the generation of robust networks (data not shown). We used a

network construction method similar to that introduced by Luthey-Schulten and co-workers (34). However, instead of employing a [4.5 Å] contact map of non-neighboring residues to define network edges (that are then weighted by a single correlation matrix), our network edges were constructed based on the minimum  $C\alpha$ - $C\alpha$  cross-correlation value between all residues across five replicate simulations. Specifically, cross-correlations were calculated for each trajectory after mass-weighted superposition. Network edges were added for (i) residue pairs with  $|c_{ij}| \geq 0.6$  in all simulations and (ii) residues satisfying  $|c_{ij}| \geq 0.6$  in at least one simulation and with a  $C\alpha$ - $C\alpha$  distance  $d_{ij} \leq 10$  Å for at least 75% of total simulation frames. Edge weights were calculated as  $-\log(|\langle c_{ij} \rangle|)$ , where  $\langle \cdot \rangle$  denotes the average across simulations. Networks constructed with a  $c_{ij}$  cutoff between 0.5 and 0.7 yielded equivalent networks with similar community structure (data not shown). This procedure was found to reduce potentially false positive couplings that exist when using only a single trajectory, as well as minimize the arbitrary exclusion of consistent strong couplings that are just beyond a given distance cutoff.

**Network Community and Centrality Analysis**—For each correlation network, hierarchical clustering was performed to generate aggregate nodal clusters, or communities, that are highly intracommunity but loosely intercommunity, using a betweenness clustering algorithm similar to that introduced by Girvan and Newman (35). However, instead of using the partition with the maximum modularity score, as is common with unweighted networks, we took the partition closest to the maximal modularity value that resulted in the smallest number of overall communities (*i.e.* the earliest high scoring partition). This avoided the common situation where many small communities with equally high scoring modularity values were generated. Using this approach networks under different states showed a largely consistent community partition, with differences localized to the nucleotide binding P-loop (PL), SI, SII, and  $\alpha 1$  regions that were observed to repartition between major communities in the different states (data not shown). Consensus communities that abstracted these regions to new separate communities to facilitate further comparisons were derived from partitioning these regions at the boundaries of their known conserved sequence motifs. Intercommunity correlations were then calculated as the sum of the mean correlation values across simulation replicates associated with all the intercommunity edges. A standard  $t$  test was also performed to measure the significance of the mean difference between intercommunity correlations of distinct states.

Node centralities that assess the density of connections per node were calculated as follows,

$$x_i = \frac{1}{\lambda} \sum_{j \in G} A_{ij} x_j \quad (\text{Eq. 2})$$

where  $x_i$  is the centrality of node  $i$ ,  $A_{ij}$  is the  $ij$ th entry of the adjusted adjacent matrix  $A$ ,  $\lambda$  is a constant to be determined, and  $G$  indicates all nodes.  $A_{ij}$  is not 0 if node  $i$  and  $j$  are linked, and it is equal to  $e^{-w_{ij}}$ , where  $w_{ij}$  is the edge weight. Solving Equation 2 for every  $i$  ( $i \in G$ ) is equivalent to finding the eigenvalues and eigenvectors of matrix  $A$ . Node centralities can then



be obtained from the eigenvector with the largest eigenvalue, after scaling all entries with the largest entry set to be 1.

**Network Path Analysis**—Given a pair of nodes treated as “source” and “sink,” respectively, optimal (shortest) and suboptimal (close to but longer than optimal) connecting network paths were identified using the algorithm in Ref. 36. Five hundred paths were collected for each source/sink pair in each network. Comparative path length distributions indicating the strength of correlated motions under distinct conditions were then calculated. In addition, normalized node degeneracy, *i.e.* the fraction of the number of paths going through each node, was calculated. Residues with high node degeneracy ( $\geq 0.1$  or 50 paths) in any network were specified as “on-path” residues and were subjected to further analysis including, for select cases, mutagenesis simulations and experimental characterization.

**Molecular Cloning**—cDNA for human adenosine A<sub>1</sub> receptor (A<sub>1</sub>R) and G $\alpha_{i2}$  isoform 1 were acquired from DNASU Plasmid Repository and Open Biosystems, respectively. N-terminal Flag-tagged G $\alpha_{i2}$  or A<sub>1</sub>R-G $\alpha_{i2}$  fusions and N-terminal mCerulean-tagged G $\alpha_{i2}$  were cloned into pBiex1 and pCDNA5/FRT plasmids, respectively. A<sub>1</sub>R and G $\alpha_{i2}$  were fused together using the previously described SPASM technique (37). Briefly, A<sub>1</sub>R-G $\alpha_{i2}$  fusions were cloned from N to C terminus as follows: A<sub>1</sub>R, mCitrine, ER/K linker, mCerulean, and G $\alpha_{i2}$ . Repeating (Gly-Ser-Gly)<sub>4</sub> sequences were inserted in between domains to ensure rotational freedom. G $\alpha_{i2}$  and G $\alpha_t$  (*Bos taurus*) residues were aligned to identify the conserved Leu<sup>32</sup>, Phe<sup>195</sup>, and Asp<sup>333</sup> residues in G $\alpha_{i2}$ . L36A, F200L, or D338A mutations in G $\alpha_{i2}$  were induced via PCR using oligonucleotide-directed mutagenesis (QuikChange site-directed mutagenesis kit; Stratagene). All constructs were confirmed via sequencing.

**Mammalian Cell Culture**—HEK293T-Flp-in (Invitrogen) cells were cultured in DMEM supplemented with 10% FBS (v/v), 4.5 g/liter D-glucose, 1% GlutaMAX, 20 mM HEPES, pH 7.5, at 37 °C in a humidified atmosphere at 5% CO<sub>2</sub>. The cells were plated at ~30% confluence into 6-well tissue cultured treated dishes. 16–20 h later, the cells were transfected with indicated construct using XtremeGene HP DNA transfection reagent. Where indicated, 24 h post-transfection, cells were incubated with 100 ng/ml pertussis toxin (PTX) for 20–24 h. Experiments were conducted when fusions or mCerulean-G $\alpha_{i2}$  constructs expressed predominately at the plasma membrane with minimal internal localization as evaluated at 20 $\times$  and 40 $\times$  magnification on a Nikon tissue culture microscope with fluorescence detection. Experiments were performed at equivalent fusion expression at a cell density of 2  $\times$  10<sup>6</sup> cells/ml. Fusion expression was quantified by measuring mCitrine and mCerulean fluorescence by exciting cells at 490 and 430 nm, respectively. Excitation and emission bandpass were correspondingly set to 8 and 4 nm. For mCerulean tagged G $\alpha_{i2}$  experiments, the cells were harvested at similar wild type and mutant G $\alpha_{i2}$  expression levels. It should be noted that wild type, F195L, and D333A expressed twice as much as L32A mutant as indicated by mCerulean fluorescence counts. Fusion integrity was evaluated by measuring mCitrine to mCerulean emission ratio. This ratio was held between 1.7 and 2.1 because mCitrine is twice as bright as mCerulean. All fluorescence measurements were con-

ducted using FlouroMax-4 fluorometer (Horiba Scientific) in an optical glass cuvette.

**Quantification of cAMP Levels**—Protocol was conducted as previously described using the cAMP Glo luminescence based assay (Promega) (38). Briefly, 28–30 h post-transfection, the cells were spun down (300 g, 3 min), resuspended at 1  $\times$  10<sup>6</sup> cells/ml in PBS solution supplemented with 0.02% glucose and 800  $\mu$ M ascorbic acid and aliquoted into 96-well round bottom opaque microplates. The cells were treated with 0.25 mM 3-isobutyl-1-methylxanthine, 1  $\mu$ M forskolin, or 10  $\mu$ M forskolin in the presence or absence of A<sub>1</sub>R agonist (12.5 nM N<sup>6</sup>-cyclopentyladenosine) for 5 min at 37 °C. After incubation with indicated compounds, the cells were lysed, and protocol was followed according to the manufacturer’s recommendations. Luminescence was recorded using a microplate luminometer (SpectraMax M5; Molecular Devices). cAMP levels (relative luminescence units) were calculated by subtracting the untransfected untreated background from the indicated conditions. Each experiment had four repeats per condition and was repeated at least three times ( $n > 12$ ).

**Insect Cell Culture and Protein Purification**—Sf9 cells were cultured and maintained in suspension with shaking at 28 °C in Sf900-II medium (Life Technologies) containing 1% Antibiotic-Antimycotic (Life Technologies). Constructs were transiently transfected into Sf9 cells using Escort IV transfection reagent (Sigma-Aldrich) in antibiotic-free medium. The cells were lysed 3 days post-transfection in HEPES lysis buffer (20 mM HEPES, pH 7.5, 0.5% Igepal, 4 mM MgCl<sub>2</sub>, 200 mM NaCl, 7% sucrose, 5 mM DTT, 50  $\mu$ g/ml PMSF, 5  $\mu$ g/ml aprotinin, 5  $\mu$ g/ml leupeptin). Lysates were clarified by ultracentrifugation (175,000  $\times$  g, 4 °C, 45 min) and bound to anti-FLAG M2 affinity resin (Sigma-Aldrich). Resin was washed with HEPES wash buffer (20 mM HEPES, pH 7.5, 150 mM KCl, 5 mM MgCl<sub>2</sub>, 5 mM DTT, 50  $\mu$ g/ml PMSF, 5  $\mu$ g/ml aprotinin, 5  $\mu$ g/ml leupeptin) and eluted using FLAG peptide (Sigma-Aldrich). Protein concentration and integrity were assessed by SDS-PAGE and Coomassie staining in comparison to BSA standards.

**Nucleotide Exchange and [<sup>35</sup>S]GTP $\gamma$ S Incorporation**—Binding of [<sup>35</sup>S]GTP $\gamma$ S to purified G $\alpha_i$  protein was based on the method outlined in Ref. 39. Briefly, the assay mixture contained 0.5  $\mu$ g of purified G $\alpha_i$  protein in TED buffer (20 mM Tris-HCl, pH 7.4, 1 mM DTT, 1 mM EDTA, 0.1 mM MgCl<sub>2</sub>) with 2  $\mu$ M GTP $\gamma$ S and 0.1 nM [<sup>35</sup>S]GTP $\gamma$ S, unless otherwise stated, in a total volume of 200  $\mu$ l. Experiments were performed at room temperature (25 °C), unless stated otherwise, and 50- $\mu$ l samples were withdrawn and diluted 1:4 in ice-cold TED buffer to stop the reaction at various time points. Aliquots were vacuum-filtered through GF/C filters, and the amount of bound radioactivity was quantified by scintillation counting. Data were analyzed using GraphPad Prism as one-phase association curves.

## Results

**GTP-, GDP-, and GDI-bound States Display Distinct Flexibilities and Dynamic Couplings in Known Functional Regions**—Five 80-ns MD simulations for each state (GTP, GDP, and GDI totaling 1.2  $\mu$ s; see “Experimental Procedures”) revealed residue fluctuations that clearly distinguished states (Fig. 2a). Specifically, the SI, SII, and SIII regions were found to

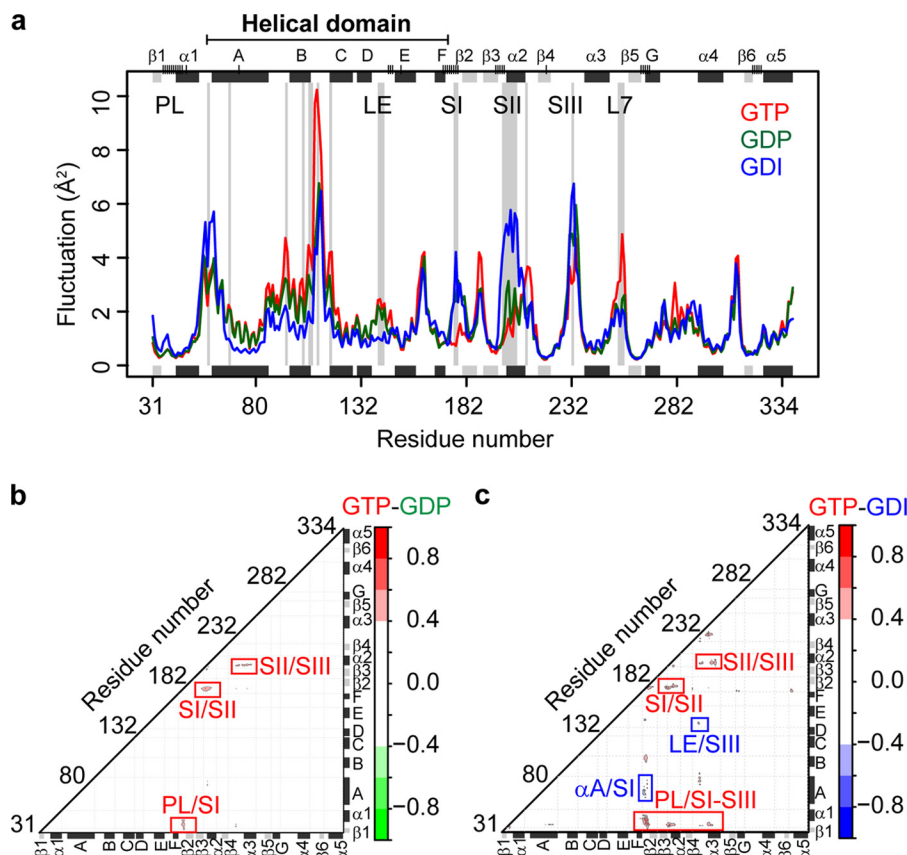
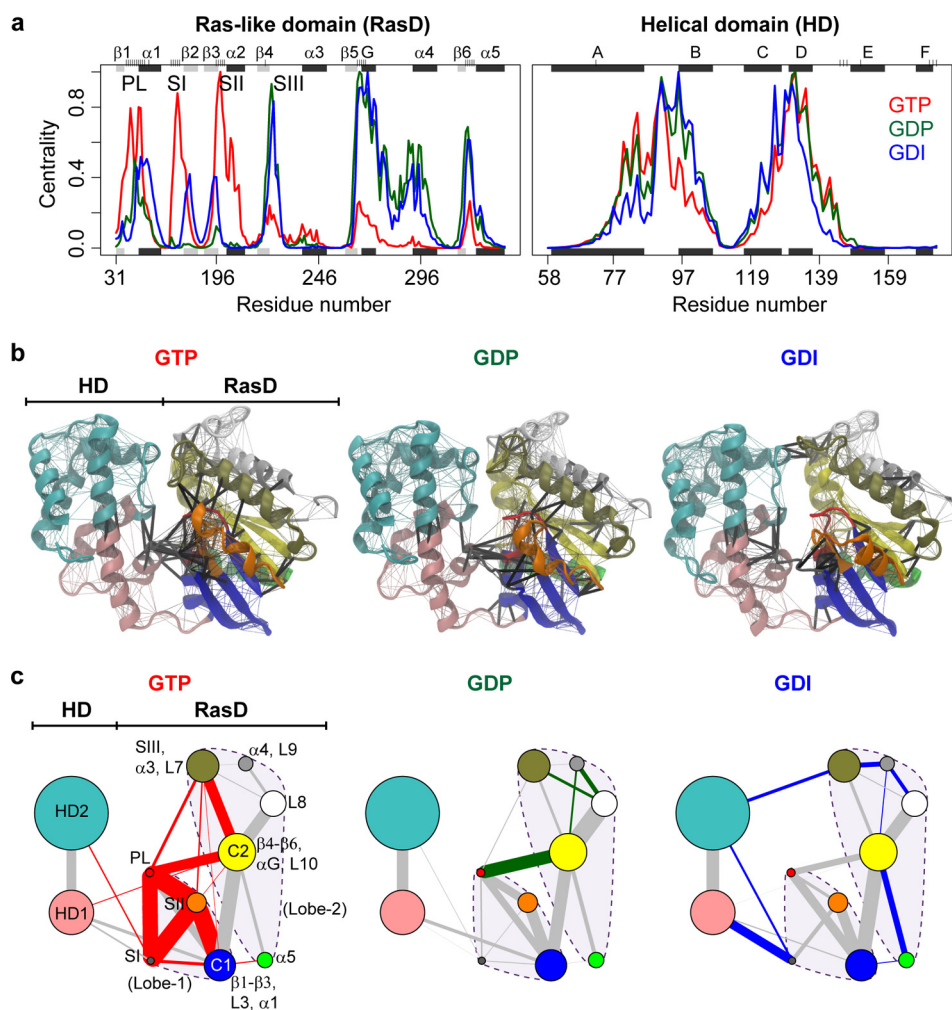


FIGURE 2. **State-specific residue fluctuations and dynamic couplings in G $\alpha$  from molecular dynamic simulations.** *a*, ensemble averaged fluctuation analysis reveals structural regions with significantly distinct flexibilities in GTP (red), GDP (green), and GDI (blue) states. Sites with a  $p$  value  $< 0.05$  are highlighted with a light gray background on the main plot. Short vertical tick lines on the top axis indicate the location of nucleotide binding site residues. Marginal black and gray rectangles indicate the location of major  $\alpha$  helix and  $\beta$  strand secondary structure elements. *b* and *c*, state-specific residue couplings. Difference correlation values between GTP and GDP (*b*) and between GTP and GDI (*c*) states are shown. Major regions displaying distinct couplings are indicated with red (GTP) and blue (GDI) labels. Note that no major GDP specific couplings were evident from comparison with GTP (*b*) or GDI (data not shown) states.

be more flexible in GDP and GDI states than in the GTP state. Conversely, a more flexible L7 region (the loop between  $\alpha 3$  and  $\beta 5$ ) was apparent for the GTP state only. The possible role of L7 in receptor binding has been suggested by both crystallographic studies (4) and mutagenesis experiments (40). Furthermore, fluctuation analysis revealed a more rigid HD region in the GDI state, with fluctuations at multiple sites predicted to be smaller in the GDI state than those in either GTP or GDP state.

MD derived residue-residue couplings also clearly distinguished GTP, GDP, and GDI states (Fig. 2, *b* and *c*). This analysis revealed that the GTP state had significantly stronger couplings in the PL and switch regions, whereas the GDI state had uniquely strong couplings around the region between RasD (SIII) and HD (the loop between  $\alpha D$  and  $\alpha E$ , or LE) and the region between  $\alpha A$  and SI (Fig. 2, *b* and *c*). It is important to note that results from a simple difference contact map analysis of trajectories did not reveal the full extent of the dynamic coupling difference reported here (data not shown). This highlights the importance of employing dynamic coupling analysis to provide additional context for the interpretation of both global and local structural dynamic changes of potential functional relevance. In the next section, we further dissect these apparent dynamic couplings with network analysis to obtain insight into potential mechanisms of long range dynamic coupling in G $\alpha$  of relevance to allostery.

*Correlation Network Analysis Further Characterizes State-specific Dynamic Couplings and Reveals the Intrinsic Dynamical Modularity of G $\alpha$* —For each state, a weighted correlation network graph was constructed from the MD simulation results. Each node of the graph represented an individual residue, and the weight of the connection between nodes was proportional to their respective correlation value calculated from multiple replicate MD simulations. To reduce noise, *i.e.* “false positive” couplings that may exist only in a single trajectory, we inspected the robustness of each coupling over multiple simulation trajectories and constructed an ensemble-averaged network with each edge representing only significant residue-residue correlations present in the entire simulation set for a given state (see “Experimental Procedures”). Eight highly connected network regions are evident in Fig. 3*a*. This analysis assesses the density of connections per node (*i.e.* node centrality) and highlights six regions in RasD and two regions in HD with a comparatively high level of coupling. Within RasD, these six regions can be equally partitioned into two major groups with the boundary located near L5 (the loop between  $\alpha 2$  and  $\beta 4$ ). These correspond to the two major lobes reported first for Ras itself using structural and evolutionary sequence analysis (24). Lobe 1, which includes all switch regions and the N-terminal half of the  $\beta$ -sheet, is highly conserved across distinct Ras isoforms, whereas lobe 2, which includes  $\alpha 3$ – $\alpha 5$  and the C-terminal half



**FIGURE 3. Correlation network analysis reveals state-specific differences in residue couplings.** *a*, node centrality values that assess the density of connections per node for RasD and HD regions in GTP (red), GDP (green), and GDI (blue) states. *b*, molecular structure mapping of consensus network communities (colored regions) and residue couplings (lines). Intercommunity couplings are indicated with thick black lines. *c*, community networks depicted with colored circles (as in *b*) whose relative radius indicates the number of residues in a particular community. The widths of linking lines are determined by their relative intercommunity coupling strength. Red-, green-, and blue-colored linking lines indicate enhanced GTP, GDP, or GDI couplings that are significantly stronger ( $p$  value < 0.005) in one state than another. All other lines are colored gray.

of the  $\beta$ -sheet, contains significant amino acid variations. Intriguingly, dynamic coupling analysis here identified the same two lobes in  $G\alpha$ , which also exhibit distinct nucleotide-dependent dynamics. In the GTP state, lobe 1 displays stronger coupling than lobe 2. Major regions of high density network connections (*i.e.* high centrality values) are located at the PL, SI, and SII. In contrast, in the GDP and GDI states, coupling in lobe 2 is stronger, and high density connections occur at SIII,  $\alpha$ G, and L10 (the loop between  $\beta$ 6 and  $\alpha$ 5). This further supports the functional relevance of the conserved bilobal substructure and reveals how nucleotide modulates the transition between active and inactive states by altering the dynamic coupling within and between these conserved structural lobes. In contrast, regions in the HD with high density connections do not show significant differences between states, indicating that changes in dynamic coupling upon nucleotide cycling are largely limited to the RasD region.

Correlation network analysis further dissects residue couplings and reveals residue communities having the potential to facilitate long range allosteric signal propagation. Clustering

was performed to define local communities of correlated residues that represent highly intraconnected but loosely interconnected substructures (see “Experimental Procedures” and Fig. 3, *b* and *c*). Consistent with centrality analysis, the RasD region can be clearly partitioned into two major lobes (Fig. 3*c*, dashed lines). Lobe 1 includes the large  $\beta$ 1– $\beta$ 3, L3, and  $\alpha$ 1 community (blue in Fig. 3, *b* and *c* and labeled “C1”) plus the PL, SI and SII elements. Lobe 2 includes the large  $\beta$ 4– $\beta$ 6,  $\alpha$ G, and L10 community (yellow in Fig. 3, *b* and *c*, labeled C2) plus four smaller communities corresponding to individual helices and their associated loops distributed on both sides of the  $\beta$ -sheet. The HD N-terminal  $\alpha$ A,  $\alpha$ E, and  $\alpha$ F were grouped into one community with the C-terminal  $\alpha$ A,  $\alpha$ B,  $\alpha$ C, and  $\alpha$ D forming a second HD community. The overall community structure reflects the intrinsic dynamic couplings within  $G\alpha$  and provides a level of abstraction at which significant commonalities and differences in potential allosteric coupling can be further understood.

Analysis of intercommunity coupling strengths reveals state-specific allosteric coupling paths and an overall dynamical tightening in the GTP state. In particular, lobe 1 couplings



## Allosteric in G Proteins

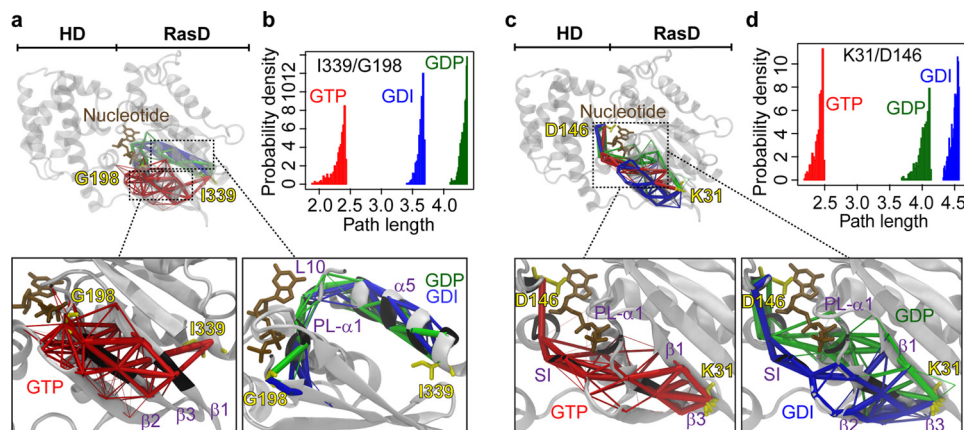


**FIGURE 4. State-specific coupling from receptor to nucleotide and helical domain interfaces.** *a*, suboptimal paths linking  $\alpha 5$  and SII for GTP (red), GDP (green), and GDI (blue) states. Line thickness scales with relative path length within a state with the shortest path rendered as the *thickest line*. Source and sink residues Ile<sup>339</sup> and Gly<sup>198</sup> are labeled and rendered in stick representation. The *bottom panels* magnify path regions and have residues with high (>0.5) node degeneracy (proportion of paths traversing a given node) colored on the protein cartoon. *b*, probability density distribution of path lengths between  $\alpha 5$  (Ile<sup>339</sup>) and SII (Gly<sup>198</sup>). *c* and *d*, suboptimal paths between  $\beta 1$  and the RasD-HD interface (with source/sink pair Lys<sup>31</sup>/Asp<sup>146</sup>) and corresponding probability density distribution of path lengths. See also [supplemental Table S2](#) for details of path analysis from receptor coordinating  $\alpha 5$  to the RasD-HD interface (with source/sink pair Ile<sup>339</sup>/Lys<sup>266</sup>).

including PL/SI, PL/SII, SI/SII, and SII/C1 are significantly enhanced in the active GTP state and weakened or absent in the inactive GDP and GDI states (Fig. 3c, red edges). Interlobe couplings to SIII ( $\alpha 3$ ) and C2 are also significantly enhanced in the GTP state. In contrast intralobe 2 couplings, including SIII/L8,  $\alpha 4$ /L8, and  $\alpha 4$ /C2 are stronger in the GDP state than those in the GTP and GDI states (Fig. 3c, green edges). Also noteworthy are the significantly stronger HD to RasD couplings evident for the GDI state (Fig. 3c, blue edges). These state-specific dynamical coupling differences are robust to variations of network model parameters and have potential implications for the nucleotide-dependent modulation of long range signal propagation. However, detailed dissection of these potential pathways and the residues involved can be better addressed with the more fine-grained path analysis approach described below together with targeted mutagenesis studies aimed at assessing their functional significance.

**Network Path Analysis Reveals Distinct Features of GTP-, GDP-, and GDI-modulated Couplings of Distal Functional Sites**—Given a pair of residues, termed source and sink, 500 suboptimal connecting coupling paths through each network were calculated. Path lengths were computed as a summation over the weights of traversed edges. Shorter paths represent stronger dynamic coupling. Source and sink pairs were chosen that represent receptor binding site to nucleotide  $\gamma$ -phosphate ( $\gamma$ -Pi) binding site (Ile<sup>339</sup>/Gly<sup>198</sup>) and receptor binding site to the RasD-HD interface (Lys<sup>31</sup>/Asp<sup>146</sup> and Ile<sup>339</sup>/Lys<sup>266</sup>; Fig. 4 and [supplemental Table S2](#)). Note that both RasD-HD interface residues, Asp<sup>146</sup> and Lys<sup>266</sup>, were chosen based on the experimental observation that significantly enhanced mobility around LE and  $\alpha G$  occurred after  $G\alpha$  activation (7). The first pair of residues is located at the C terminus of  $\alpha 5$  and the  $\gamma$ -Pi coordinating SII region, respectively. For the GTP state, calculated paths predominantly traversed the lobe 1  $\beta$ -strands ( $\beta 1$ ,  $\beta 2$ , and  $\beta 3$ ), whereas in the GDP and GDI states the dominant paths involved  $\alpha 5$ ,  $\alpha 1$ , and L10 from lobe 2 (Fig. 4a). Examining the distributions of path lengths indicated that the GTP state had much shorter overall paths (Fig. 4b). This is indicative of

the apparent dynamical tightening of the lobe 1 region in the active state evident from network community analysis (Fig. 3, b and c). Paths from receptor coordinating  $\beta 1$  (Lys<sup>31</sup>) to the RasD-HD interface (Asp<sup>146</sup>) displayed differing favored routes in distinct states. In the GTP network, paths mainly traversed  $\beta 1$ ,  $\beta 3$ , SI, and PL, whereas in the GDI network, the traversed regions extended to  $\beta 2$  but excluded PL (Fig. 4c). In the GDP network, the traversing region was mainly  $\beta 1$ ,  $\beta 3$ , PL, and  $\alpha 1$  (Fig. 4c). Moreover, the path length distributions show that the GTP state had much shorter paths than either GDP or GDI state, again demonstrating the dynamical tightening of the active state (Fig. 4d). Path analysis from receptor coordinating  $\alpha 5$  (Ile<sup>339</sup>) to RasD-HD interface (Lys<sup>266</sup>) revealed a common major route through  $\alpha 5$ -L10- $\alpha G$  ([supplemental Table S2](#)) and similar path length distributions across GTP, GDP, and GDI states (data not shown). This indicates that the  $\beta 1$ -HD pathway is more dynamic during G protein cycling and potentially more sensitive to external modulations such as small molecule binding and point mutations.

Normalized network node degeneracy, which characterizes the percentage of total paths that traverse a given node, revealed that many high degeneracy residues are also highly conserved in sequence ([supplemental Table S2](#)). Furthermore, previous *in vitro* mutagenesis of predicted on-path residues (occurring on >10% of total paths) indicates that many are functionally relevant. In particular, point mutations of residues from SI (Arg<sup>174</sup> and Thr<sup>177</sup>),  $\beta 3$  (Phe<sup>192</sup>), L10 (Cys<sup>321</sup>), and  $\alpha 5$  (Asn<sup>327</sup>, Val<sup>328</sup>, Phe<sup>330</sup>, Val<sup>331</sup>, Phe<sup>332</sup>, Asp<sup>337</sup>, Ile<sup>338</sup>, and Ile<sup>339</sup>) have shown significantly altered basal and receptor-catalyzed nucleotide exchange rates (13, 17, 41, 42). All of these residues are characterized as playing a prominent role in coupling paths linking receptor-binding and domain-binding interfaces (*i.e.* high node degeneracy values; [supplemental Table S2](#)). Below we explore further how perturbations, introduced via point mutations, can potentially affect these apparent coupling networks.

**On Path Mutations Promote Domain Opening and Disrupt Long range Couplings Linked to Receptor-catalyzed Nucleotide Exchange**—Five replicate 80-ns GTP-bound MD simulations and subsequent network analysis were performed on each of

five mutant variants: L32A, F195L, F332A, D333A and I339A. These positions were highlighted by path analysis as contributing to the coupling of receptor, nucleotide and HD binding interfaces. The highly conserved  $\alpha 5$  residue Ile<sup>339</sup> and  $\beta 1$  residue Leu<sup>32</sup> were identified as key mediators of GTP specific couplings between  $\alpha 5$  and the  $\beta$ -sheet (Fig. 4a and supplemental Table S2). The  $\beta 3$  residue Phe<sup>195</sup> was predicted to participate in the coupling paths between  $\beta 1$  and the RasD-HD interface (supplemental Table S2). We note that a leucine substitution at an equivalent position in  $G\alpha_2$  has been reported to be associated with ventricular tachycardia (43). The conserved residue Phe<sup>332</sup> in  $\alpha 5$  was identified to participate in the paths between  $\alpha 5$  and RasD-HD interface (supplemental Table S2), and substitution of an equivalent position in  $G\alpha 11$  has been reported to be associated with hypocalcemia (44). The importance of Phe<sup>332</sup> on nucleotide exchange has also been demonstrated in both *in vitro* experiments and computational energetic analysis (13, 17, 45, 46). The  $\alpha 5$  residue Asp<sup>333</sup> is solvent-exposed and not directly involved in contact with other structural elements outside of  $\alpha 5$  but is predicted here to be a prominent on-path site (supplemental Table S2).

Our MD simulations of L32A, F332A, and I339A showed a substantial effect on the rate of RasD-HD domain opening. Specifically, these mutants displayed a 200-fold more populated open conformation than wild type during equivalent simulations (Fig. 5a). These mutants also displayed  $C\alpha$ -based root mean square deviation from the initial structure of up to 5–6 Å, because of this relative domain opening. Interestingly, the D333A mutant simulations under the same conditions displayed a similar level of domain opening to that of wild type, whereas F195L showed a more moderate level of enhanced domain opening (Fig. 5a). Network path analysis indicated that the mutants with the most perturbed coupling paths (D333A and F195L) displayed the least domain opening events. Conversely, mutants with relatively unperturbed coupling paths (L32A, F332A, and I339A) displayed enhanced opening. This suggests that mutations mimicking the effect of receptor binding may utilize wild type-like coupling paths for eliciting their allosteric effect on domain opening. Detailed inspection further revealed that only D333A and F195L mutations displaced on-path residues, most notably the SI region, leading to elongated path lengths. Collectively, these results indicate that both path analysis and subsequent mutant simulations are required for prediction of the structural dynamic effects of mutation. Our predictions parallel previous *in vitro* experimental measurements of enhanced spontaneous nucleotide exchange rates for mutations equivalent to F332A and I339A (13, 17). The current results indicate that enhanced domain opening can lead to enhanced nucleotide exchange. However, currently very little is known experimentally about the potential allosteric role or effect of mutations at sites Leu<sup>32</sup> and Asp<sup>333</sup>.

*G $\alpha_i$  Signaling Properties Are Modulated by the Predicted Single Point Mutations That Act Allosterically*—To examine the effect of our potential receptor-decoupling  $G\alpha_i$  mutants, we experimentally assayed cAMP levels in HEK293 cells using the recently described SPASM GPCRs construct (see “Experimental Procedures” and Ref. 37). Briefly, adenosine type 1 receptor (A<sub>1</sub>R) was fused to the N terminus of wild type or mutant  $G\alpha_i$

using the SPASM module. At equivalent expression levels, measurements were performed in the presence and absence of the adenylyl cyclase activator, forskolin (Fsk), and adenosine receptor agonist, N<sup>6</sup>-cyclopentyladenosine in live cells (Fig. 5c). As expected, Fsk addition increased cAMP levels compared with basal for all systems. However, the relative magnitude of this increase differs between mutants and wild type (Fig. 5c, *dashed bars*), as does the relative reduction of Fsk-stimulated cAMP levels upon agonist addition (Fig. 5c, *dashed versus filled bars*). Treatment with Fsk alone resulted in a 1.6, 1.2, 0.4, and –0.3-fold increase in cAMP levels for wild type, F195L, D333A, and L32A mutants, respectively, compared with untransfected cells (Fig. 5c, *dashed bars*). The reduced basal cAMP levels for D333A and L32A compared with untransfected and wild type indicate an enhanced level of G<sub>i</sub> activity for these mutants even in the absence of receptor stimulation (agonist free conditions; Fig. 5c, *open bars*). Furthermore, for L32A agonist addition had little effect on Fsk-stimulated cAMP levels indicating that this mutant, and to a lesser extent D333A, are constitutively active and do not require agonist stimulated receptor to exert their effect on adenylyl cyclase. The constitutive activities of L32A and D333A were also supported by independent PTX experiments. PTX inhibits GPCR-mediated activation of G<sub>i</sub> (47). The cAMP levels for D333A and L32A mutants were much lower than that for wild type even after PTX inhibition (Fig. 5, *d* and *e*). We note that D333A displays more moderate activity than L32A in the absence of receptor agonist (Fig. 5c). This is consistent with its predicted reduced domain opening activity relative to L32A (Fig. 5a). However, it is important to note that our accessible simulation time (5 × 80 ns) likely provides only a partial characterization of these rare events for such mutants. In such cases, enhanced sampling methods, such as accelerated MD, may provide additional insight as we have previously demonstrated (3).

Binding of the nonhydrolyzable GTP analogue [<sup>35</sup>S]GTP $\gamma$ S (48) to  $G\alpha_i$  was used to compare nucleotide binding to L32A and WT. Steady state levels of [<sup>35</sup>S]GTP $\gamma$ S binding were the same in both L32A and WT, but the rate of association at 25 °C was faster in the L32A ( $t_{1/2} = 12.9 \pm 2.6$  min) than the WT ( $t_{1/2} = 19.1 \pm 2.5$  min;  $p = 0.04$ , paired *t* test) (Fig. 5f). In an additional experiment at 37 °C using 0.4 nM [<sup>35</sup>S]GTP $\gamma$ S, rates of association were faster, but a similar difference was seen between L32A ( $t_{1/2} = 1.8$  min) and WT ( $t_{1/2} = 5.3$  min). These results are consistent with both cAMP assays (Fig. 5c) and MD simulations (Fig. 5a) and reveal the faster GTP binding kinetics of L32A.

## Discussion

Our extensive MD simulations predicted nucleotide-dependent modes of motion and internal dynamic coupling of functional regions including SI, SII, SIII, PL, and HD. Correlation network analysis characterized the conserved bilobal dynamic substructure of RasD reminiscent of that observed in Ras itself. Nucleotide turnover led to a modulation of the coupling between these substructures with an overall dynamical tightening in the GTP state and enhanced HD-RasD couplings in the GDI state. Network path analysis and subsequent mutant simulations highlighted residues of potential importance for the coordination of receptor and nucleotide-binding site to the



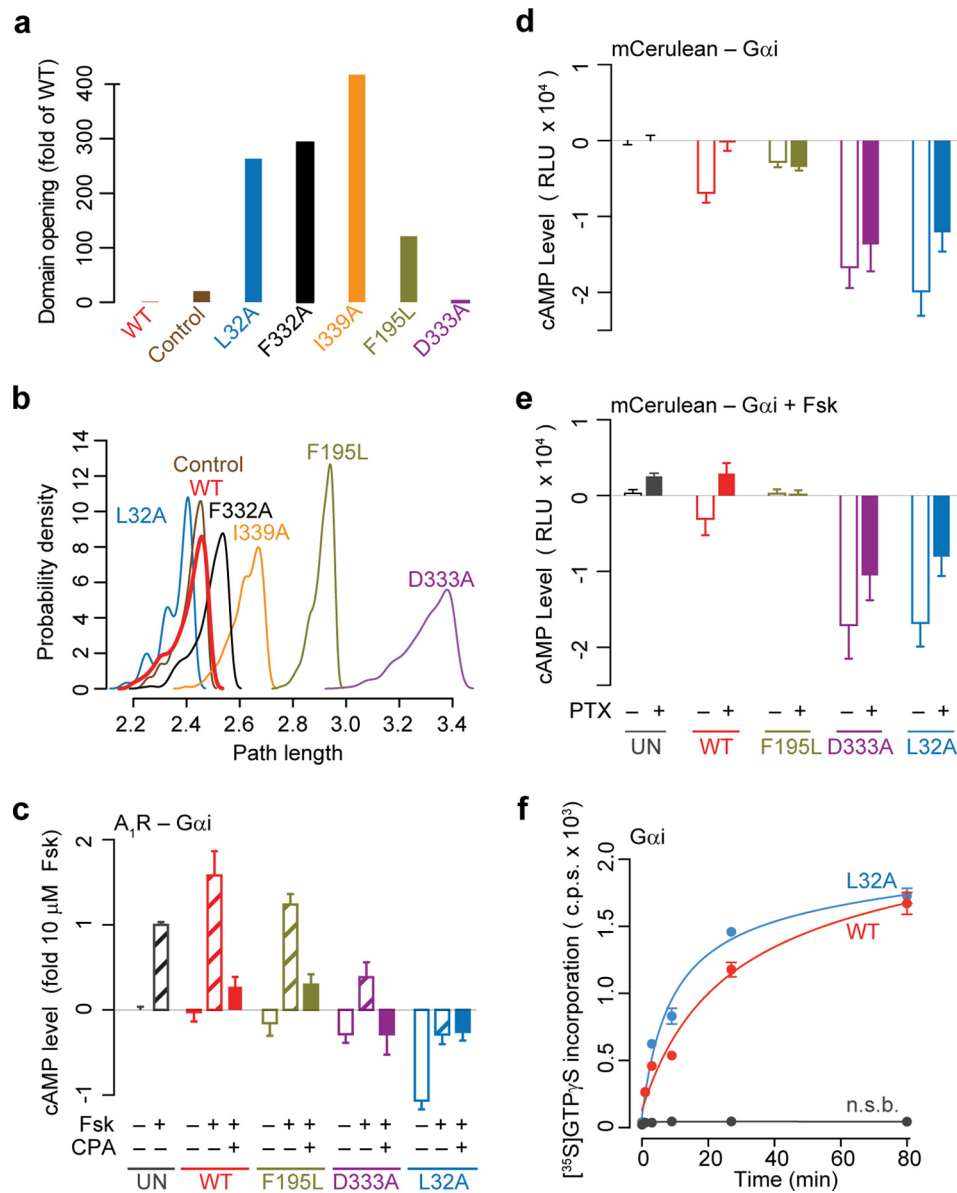


FIGURE 5. **Computational and experimental mutagenesis of on path residues.** *a*, fraction of domain opening events observed relative to WT simulations for L32A, F195L, F332A, D333A, and I339A. The same WT simulation protocols and network analysis methods were implemented for all mutant simulations. Domain opening was detected whenever the minimum C $\alpha$ -C $\alpha$  distance between LE (on the HD side) and SIII (on RasD) exceeded 10 Å in the cumulative 5 × 80-ns simulations. *Control* refers to a set of five separately performed WT simulations. Note that all simulations were structurally stable as indicated by standard geometric analysis (data not shown). *b*, probability density distribution of path lengths from receptor coordinating  $\beta$ 1 (Lys<sup>31</sup>) to RasD-HD interface (Asp<sup>146</sup>) in WT and mutants. *c*, cAMP levels for the WT and mutant A<sub>1</sub>R-G $\alpha$ <sub>i</sub> fusions for indicated conditions in live HEK293 cells (Untransfected (UN), 10 μM Fsk, and 12.5 nM N<sup>6</sup>-cyclopentyladenosine (CPA, A<sub>1</sub>R agonist)). *d* and *e*, cAMP levels for HEK293 cells expressing WT or mutant mCerulean labeled G $\alpha$ <sub>i</sub>, treated without (*d*) or with (*e*) forskolin (10 μM Fsk) in the presence or absence of PTX. PTX treatment inhibits WT but not D333A and L32A activity, indicating that the latter display receptor-independent constitutive activity. *f*, representative time course of [<sup>35</sup>S]GTPγS binding to purified WT and L32A mutant G $\alpha$ <sub>i</sub>. *n.s.b.*, nonspecific binding.

RasD-HD interface. In particular, the on-path mutation D333A displayed disrupted dynamic coupling between distal functional sites, whereas L32A, F332A, and I339A led to an enhanced helical domain opening. Experimental characterization of D333A and L32A revealed constitutive activity in the absence of receptor supporting the functional relevance of these allosteric mutations. Mutations of the additionally highlighted Phe<sup>332</sup> and Ile<sup>339</sup> have been shown previously to result in enhanced spontaneous rates of nucleotide exchange (13, 17).

Recent alanine scanning mutagenesis and thermostability assays by Sun *et al.* (46) identified clusters of hydrophobic res-

idues that confer differential stability to GDP-, GTPγS-, and rhodopsin-bound G $\alpha$ <sub>i1</sub>. In particular, residues in  $\alpha$ 5 (most notably Phe<sup>336</sup>, which is equivalent to our Phe<sup>332</sup>),  $\alpha$ 1 (including Ile<sup>49</sup>, Gln<sup>52</sup>, and Met<sup>53</sup>), and  $\beta$ 1 (Leu<sup>38</sup> equivalent to Leu<sup>34</sup>, which is a neighboring residue to our Leu<sup>32</sup>) were found to confer greater thermal stability to GDP- and GTPγS-bound states. Importantly, F336A was revealed to be the only substitution that resulted in both loss of stability and altered nucleotide binding kinetics. Using independent biophysical modeling, we report here that this substitution results in increased domain opening rates. This provides a clear structural

dynamic perspective consistent with the previous finding that this mutation increases the rate of nucleotide release (17). In a similar manner, we report that the novel L32A mutation results in enhanced helical domain opening, increased nucleotide binding rates, and constitutive activity in the absence of receptor.

Using differential contact analysis of  $G\alpha$  crystal structure subsets, Flock *et al.* (49) recently suggested that structural contacts between  $\alpha 1$  and  $\alpha 5$  act as a “hub” for  $G\alpha$  allosteric activation. In this model, activation is mediated by the breaking of contacts between  $\alpha 5$  and  $\alpha 1$ , leading to an increased flexibility of  $\alpha 1$  that promotes GDP release. The allosteric importance of  $\alpha 5$  was also highlighted in recent long time scale MD simulations by Dror *et al.* (10). These simulations suggested that  $\alpha 5$  displacement upon receptor binding results in an increased flexibility of the  $\beta 6$ - $\alpha 5$  loop. This loop, located at the N terminus of  $\alpha 5$ , coordinates the guanosine moiety of a bound nucleotide. Interestingly, Flock *et al.* state that residues contacting the guanosine moiety, including the  $\beta 6$ - $\alpha 5$  “are not extensively reorganized during  $G\alpha$  activation.” In both the Flock *et al.* and Dror *et al.* models,  $\alpha 5$  acts as the primary initial conduit of information transfer between the receptor and nucleotide binding sites. The models differ in that Dror *et al.* propose that flexibility differences of the  $\beta 6$ - $\alpha 5$  loop complete the connection to the guanosine moiety, whereas Flock *et al.* propose that increased  $\alpha 1$  dynamics is the primary determinant of allosteric coupling. Our path analysis results support the importance of  $\alpha 5$  in general and the  $\beta 6$ - $\alpha 5$  loop in particular (Dror *et al.* model). However, we provide new evidence for a dominant alternate allosteric coupling route through  $\beta 1$  that directly links from receptor to the phosphate coordinating P-loop. Both the C-terminal of  $\alpha 5$  and the N-terminal  $\beta 1$  are known GPCR binding interfaces. The increased dynamics of both regions upon receptor binding were also evident in earlier hydrogen/deuterium exchange data (7). Moreover, our analysis of the structural dynamic effects of mutations in these regions reveals the novel role of  $\beta 1$  together with  $\beta 2$ ,  $\beta 3$ , P-loop, and SI in the regulation of domain opening that is critical for nucleotide exchange.

More frequent RasD-HD domain separation has previously been suggested to underlie the self-activation of the G protein GPA1 from *Arabidopsis thaliana* (9). GPA1 is permanently activated, has enhanced nucleotide exchange rates, and displays enhanced domain opening in simulations relative to  $G\alpha_i$ . Intriguingly, investigations of chimeric proteins established that the HD  $\alpha A$  helix of GPA1 is almost entirely responsible for this enhanced activation. We note that the  $\alpha A$  helix spans the two major HD communities (Fig. 3, *b* and *c*) and that perturbations to  $\alpha A$  have the potential to effect dynamic couplings in the entire HD region. Collectively, our mutational analysis and the GPA1 chimeric analysis indicate that sites distant from regions involved in binding to receptors, effectors, and nucleotides can perturb the structural dynamics and function of G proteins.

Our results indicate that network analysis of dynamic couplings from multiple replicate MD simulations is a promising method to delineate features of protein allostery. Similar network approaches have been successfully applied to a number

of important biological systems (3, 34, 50–54). The major improvement in our current implementation *versus* our previous work (3, 52, 53) and that of others is the use of many multiple replicate trajectories instead of results from single simulations. This reduces statistical errors in the calculated cross-correlation matrix and resulting correlation network and importantly allows for a more robust statistical assessment of within state and between state dynamic coupling differences. It is important to note that this widely applicable approach provides structural and dynamic insights that are not immediately available from accumulated crystal structures or individual pairs of trajectories. Furthermore, combining this approach with targeted computational and experimental mutagenesis lays the foundation for dissecting the dynamic consequences of disease-associated mutations and the potential generality of allosteric coupling mechanisms in related GTPase and ATPase systems.

**Author Contributions**—B. J. G., X.-Q. Y., S. S., and J. R. T. designed the study. X.-Q. Y. and B. J. G. performed and analyzed the MD simulations. R. M. and N. W. G. performed and analyzed the experiment. X.-Q. Y., B. J. G., and L. S. developed methods for the computational modeling and analysis. All authors reviewed the results and wrote the manuscript.

**Acknowledgments**—We thank Drs. G. Scarabelli and J. Tesmer for valuable discussions.

## References

1. Neves, S. R., Ram, P. T., and Iyengar, R. (2002) G protein pathways. *Science* **296**, 1636–1639
2. Sprang, S. R. (1997) G protein mechanisms: insights from structural analysis. *Annu. Rev. Biochem.* **66**, 639–678
3. Yao, X.-Q., and Grant, B. J. (2013) Domain-opening and dynamic coupling in the  $\alpha$ -subunit of heterotrimeric G proteins. *Biophys. J.* **105**, L08–10
4. Rasmussen, S. G., DeVree, B. T., Zou, Y., Kruse, A. C., Chung, K. Y., Kobilka, T. S., Thian, F. S., Chae, P. S., Pardon, E., Calinski, D., Mathiesen, J. M., Shah, S. T., Lyons, J. A., Caffrey, M., Gellman, S. H., Steyaert, J., Skiniotis, G., Weis, W. I., Sunahara, R. K., and Kobilka, B. K. (2011) Crystal structure of the  $\beta 2$  adrenergic receptor-Gs protein complex. *Nature* **477**, 549–555
5. Westfield, G. H., Rasmussen, S. G., Su, M., Dutta, S., DeVree, B. T., Chung, K. Y., Calinski, D., Velez-Ruiz, G., Oleskie, A. N., Pardon, E., Chae, P. S., Liu, T., Li, S., Woods, V. L., Jr., Steyaert, J., Kobilka, B. K., Sunahara, R. K., and Skiniotis, G. (2011) Structural flexibility of the  $G\alpha_s$   $\alpha$ -helical domain in the  $\beta 2$ -adrenoceptor Gs complex. *Proc. Natl. Acad. Sci. U.S.A.* **108**, 16086–16091
6. Van Eps, N., Preininger, A. M., Alexander, N., Kaya, A. I., Meier, S., Meiler, J., Hamm, H. E., and Hubbell, W. L. (2011) Interaction of a G protein with an activated receptor opens the interdomain interface in the  $\alpha$  subunit. *Proc. Natl. Acad. Sci. U.S.A.* **108**, 9420–9424
7. Chung, K. Y., Rasmussen, S. G., Liu, T., Li, S., DeVree, B. T., Chae, P. S., Calinski, D., Kobilka, B. K., Woods, V. L., Jr., and Sunahara, R. K. (2011) Conformational changes in the G protein  $G_s$  induced by the  $\beta 2$  adrenergic receptor. *Nature* **477**, 611–615
8. Jones, J. C., Duffy, J. W., Machius, M., Temple, B. R., Dohlman, H. G., and Jones, A. M. (2011) The crystal structure of a self-activating G protein  $\alpha$  subunit reveals its distinct mechanism of signal initiation. *Sci. Signal.* **4**, ra8
9. Jones, J. C., Jones, A. M., Temple, B. R., and Dohlman, H. G. (2012) Differences in intradomain and interdomain motion confer distinct activation properties to structurally similar  $G\alpha$  proteins. *Proc. Natl. Acad. Sci. U.S.A.* **109**, 7275–7279

10. Dror, R. O., Mildorf, T. J., Hilger, D., Manglik, A., Borhani, D. W., Arlow, D. H., Philippsen, A., Villanueva, N., Yang, Z., Lerch, M. T., Hubbell, W. L., Kobilka, B. K., Sunahara, R. K., and Shaw, D. E. (2015) Structural basis for nucleotide exchange in heterotrimeric G proteins. *Science* **348**, 1361–1365
11. Oldham, W. M., and Hamm, H. E. (2008) Heterotrimeric G protein activation by G-protein-coupled receptors. *Nat. Rev. Mol. Cell Biol.* **9**, 60–71
12. Iiri, T., Herzmark, P., Nakamoto, J. M., van Dop, C., and Bourne, H. R. (1994) Rapid GDP release from G $\alpha$  in patients with gain and loss of endocrine function. *Nature* **371**, 164–168
13. Marin, E. P., Krishna, A. G., and Sakmar, T. P. (2001) Rapid activation of transducin by mutations distant from the nucleotide-binding site: evidence for a mechanistic model of receptor-catalyzed nucleotide exchange by G proteins. *J. Biol. Chem.* **276**, 27400–27405
14. Kapoor, N., Menon, S. T., Chauhan, R., Sachdev, P., and Sakmar, T. P. (2009) Structural evidence for a sequential release mechanism for activation of heterotrimeric G proteins. *J. Mol. Biol.* **393**, 882–897
15. Preininger, A. M., Funk, M. A., Oldham, W. M., Meier, S. M., Johnston, C. A., Adhikary, S., Kimple, A. J., Siderovski, D. P., Hamm, H. E., and Iverson, T. M. (2009) Helix dipole movement and conformational variability contribute to allosteric GDP release in G $\alpha$  subunits. *Biochemistry* **48**, 2630–2642
16. Thaker, T. M., Sarwar, M., Preininger, A. M., Hamm, H. E., and Iverson, T. M. (2014) A transient interaction between the phosphate binding loop and switch I contributes to the allosteric network between receptor and nucleotide in G $\alpha_{11}$ . *J. Biol. Chem.* **289**, 11331–11341
17. Kaya, A. I., Lokits, A. D., Gilbert, J. A., Iverson, T. M., Meiler, J., and Hamm, H. E. (2014) A conserved phenylalanine as relay between the  $\alpha 5$  helix and the GDP binding region of heterotrimeric G $_i$  protein  $\alpha$  subunit. *J. Biol. Chem.* **289**, 24475–24487
18. Grant, B. J., Rodrigues, A. P., ElSawy, K. M., McCammon, J. A., and Caves, L. S. (2006) Bio3d: an R package for the comparative analysis of protein structures. *Bioinformatics* **22**, 2695–2696
19. Skjaerven, L., Yao, X. Q., Scarabelli, G., and Grant, B. J. (2014) Integrating protein structural dynamics and evolutionary analysis with Bio3D. *BMC Bioinformatics* **15**, 399
20. Humphrey, W., Dalke, A., and Schulten, K. (1996) VMD: visual molecular dynamics. *J. Mol. Graph.* **14**, 33–38
21. Berman, H. M., Westbrook, J., Feng, Z., Gilliland, G., Bhat, T. N., Weissig, H., Shindyalov, I. N., and Bourne, P. E. (2000) The Protein Data Bank. *Nucleic Acids Res.* **28**, 235–242
22. Gerstein, M., and Altman, R. B. (1995) Average core structures and variability measures for protein families: application to the immunoglobulins. *J. Mol. Biol.* **251**, 161–175
23. Caves, L. S., Evanseck, J. D., and Karplus, M. (1998) Locally accessible conformations of proteins: multiple molecular dynamics simulations of crambin. *Protein Sci.* **7**, 649–666
24. Gorfie, A. A., Grant, B. J., and McCammon, J. A. (2008) Mapping the nucleotide and isoform-dependent structural and dynamical features of Ras proteins. *Structure* **16**, 885–896
25. Grant, B. J., McCammon, J. A., Caves, L. S., and Cross, R. A. (2007) Multivariate analysis of conserved sequence-structure relationships in kinases: coupling of the active site and a tubulin-binding sub-domain. *J. Mol. Biol.* **368**, 1231–1248
26. van Aalten, D. M., Conn, D. A., de Groot, B. L., Berendsen, H. J., Findlay, J. B., and Amadei, A. (1997) Protein dynamics derived from clusters of crystal structures. *Biophys. J.* **73**, 2891–2896
27. Case, D. A., Darden, T. A., Cheatham, T. E. I. I. I., Simmerling, C. L., Wang, J., Duke, R. E., Luo, R., Walker, R. C., Zhang, W., Merz, K. M., Roberts, B., Hayik, S., Roitberg, A., Seabra, G., Wails, J., Goetz, A. W., Kolossvary, I., Wong, K. F., Paesani, F., Vanicek, J., Wolf, R. M., Liu, J., Wu, X., Brozell, S. R., Steinbrecher, T., Gohlke, H., Cai, Q., Ye, X., Hsieh, M. J., Cui, G., Roe, D. R., Mathews, D. H., Seetin, M. G., Salomon-Ferrer, R., Sagui, C., Babin, V., Luchko, T., Gusarov, S., Kovalenko, A., and Kollman, P. A. (2012) AMBER 12, University of California, San Francisco, CA
28. Hornak, V., Abel, R., Okur, A., Strockbine, B., Roitberg, A., and Simmerling, C. (2006) Comparison of multiple Amber force fields and development of improved protein backbone parameters. *Proteins* **65**, 712–725
29. Meagher, K. L., Redman, L. T., and Carlson, H. A. (2003) Development of polyphosphate parameters for use with the AMBER force field. *J. Comput. Chem.* **24**, 1016–1025
30. Li, H., Robertson, A. D., and Jensen, J. H. (2005) Very fast empirical prediction and rationalization of protein pKa values. *Proteins* **61**, 704–721
31. Ichiye, T., and Karplus, M. (1991) Collective motions in proteins: a covariance analysis of atomic fluctuations in molecular dynamics and normal mode simulations. *Proteins* **11**, 205–217
32. Dubay, K. H., Bothma, J. P., and Geissler, P. L. (2011) Long-range intra-protein communication can be transmitted by correlated side-chain fluctuations alone. *PLoS Comput. Biol.* **7**, e1002168
33. Wu, S., Jun Lee, C., and Pedersen, L. G. (2014) Analysis on long-range residue-residue communication using molecular dynamics. *Proteins* **82**, 2896–2901
34. Sethi, A., Eargle, J., Black, A. A., and Luthey-Schulten, Z. (2009) Dynamical networks in tRNA:protein complexes. *Proc. Natl. Acad. Sci. U.S.A.* **106**, 6620–6625
35. Girvan, M., and Newman, M. E. (2002) Community structure in social and biological networks. *Proc. Natl. Acad. Sci. U.S.A.* **99**, 7821–7826
36. Yen, J. Y. (1971) Finding K shortest loopless paths in a network. *Management Science Series A-Theory* **17**, 712–716
37. Malik, R. U., Ritt, M., DeVree, B. T., Neubig, R. R., Sunahara, R. K., and Sivaramakrishnan, S. (2013) Detection of G protein-selective G protein-coupled receptor (GPCR) conformations in live cells. *J. Biol. Chem.* **288**, 17167–17178
38. Gabriel, D., Vernier, M., Pfeifer, M. J., Dasen, B., Tenaillon, L., and Bouhelal, R. (2003) High throughput screening technologies for direct cyclic AMP measurement. *Assay Drug Dev. Technol.* **1**, 291–303
39. Slepak, V. Z., Wilkie, T. M., and Simon, M. I. (1993) Mutational analysis of G protein  $\alpha$  subunit G $_{\alpha}$  expressed in *Escherichia coli*. *J. Biol. Chem.* **268**, 1414–1423
40. Grishina, G., and Berlot, C. H. (2000) A surface-exposed region of G $_{\alpha}$  in which substitutions decrease receptor-mediated activation and increase receptor affinity. *Mol. Pharmacol.* **57**, 1081–1092
41. Nishina, H., Nimota, K., Kukimoto, I., Maehama, T., Takahashi, K., Hoshino, S., Kanaho, Y., and Katada, T. (1995) Significance of Thr182 in the nucleotide-exchange and GTP-hydrolysis reactions of the  $\alpha$  subunit of GTP-binding protein Gi2. *J. Biochem.* **118**, 1083–1089
42. Thomas, T. C., Schmidt, C. J., and Neer, E. J. (1993) G-protein  $\alpha$  subunit: mutation of conserved cysteines identifies a subunit contact surface and alters GDP affinity. *Proc. Natl. Acad. Sci. U.S.A.* **90**, 10295–10299
43. Lerman, B. B., Dong, B., Stein, K. M., Markowitz, S. M., Linden, J., and Catanzaro, D. F. (1998) Right ventricular outflow tract tachycardia due to a somatic cell mutation in G protein subunit  $\alpha_2$ . *J. Clin. Invest.* **101**, 2862–2868
44. Nesbit, M. A., Hannan, F. M., Howles, S. A., Babinsky, V. N., Head, R. A., Cranston, T., Rust, N., Hobbs, M. R., Heath, H., 3rd, and Thakker, R. V. (2013) Mutations affecting G-protein subunit  $\alpha 11$  in hypercalcemia and hypocalcemia. *N. Engl. J. Med.* **368**, 2476–2486
45. Alexander, N. S., Preininger, A. M., Kaya, A. I., Stein, R. A., Hamm, H. E., and Meiler, J. (2014) Energetic analysis of the rhodopsin-G-protein complex links the  $\alpha 5$  helix to GDP release. *Nat. Struct. Mol. Biol.* **21**, 56–63
46. Sun, D., Flock, T., Deupi, X., Maeda, S., Matkovic, M., Mendieta, S., Mayer, D., Dawson, R. J., Schertler, G. F., Babu, M. M., and Vepintsev, D. B. (2015) Probing G $\alpha_{11}$  protein activation at single-amino acid resolution. *Nat. Struct. Mol. Biol.* **22**, 686–694
47. Locht, C., Coutte, L., and Mielcarek, N. (2011) The ins and outs of pertussis toxin. *FEBS J.* **278**, 4668–4682
48. Harrison, C., and Traynor, J. R. (2003) The [35S]GTP $\gamma$ S binding assay: approaches and applications in pharmacology. *Life Sci.* **74**, 489–508
49. Flock, T., Ravarani, C. N., Sun, D., Venkatakrishnan, A. J., Kayikci, M., Tate, C. G., Vepintsev, D. B., and Babu, M. M. (2015) Universal allosteric mechanism for G $\alpha$  activation by GPCRs. *Nature* **524**, 173–179
50. Vanwart, A. T., Eargle, J., Luthey-Schulten, Z., and Amaro, R. E. (2012) Exploring residue component contributions to dynamical network models of allostery. *J. Chem. Theory Comput.* **8**, 2949–2961



51. Gasper, P. M., Fuglestad, B., Komives, E. A., Markwick, P. R., and McCammon, J. A. (2012) Allosteric networks in thrombin distinguish procoagulant vs. anticoagulant activities. *Proc. Natl. Acad. Sci. U.S.A.* **109**, 21216–21222
52. Scarabelli, G., and Grant, B. J. (2013) Mapping the structural and dynamical features of kinesin motor domains. *PLoS Comput. Biol.* **9**, e1003329
53. Scarabelli, G., and Grant, B. J. (2014) Kinesin-5 allosteric inhibitors uncouple the dynamics of nucleotide, microtubule, and neck-linker binding sites. *Biophys. J.* **107**, 2204–2213
54. Guo, J., Pang, X., and Zhou, H.-X. (2015) Two pathways mediate interdomain allosteric regulation in Pin1. *Structure* **23**, 237–247

## Supplemental Information

### Dynamic coupling and allosteric networks in the alpha subunit of heterotrimeric G proteins

Xin-Qiu Yao<sup>a,1</sup>, Rabia Malik<sup>b,e,1</sup>, Nicholas W. Griggs<sup>c</sup>, Lars Skjærven<sup>d</sup>, John R. Traynor<sup>c</sup>, Sivaraj Sivaramakrishnan<sup>e</sup>, and Barry J. Grant<sup>a,2</sup>

<sup>a</sup>Department of Computational Medicine and Bioinformatics, <sup>b</sup>Department of Cell and Developmental Biology, and <sup>c</sup>Department of Pharmacology, University of Michigan, Ann Arbor, Michigan, 48109 USA.

<sup>d</sup>Department of Biomedicine, University of Bergen, Norway.

<sup>e</sup>Department of Genetics, Cell Biology, and Development, University of Minnesota, Minneapolis, MN 55455, USA.

<sup>1</sup>Equal contributions

<sup>2</sup>Correspondence to B. J. Grant  
100 Washtenaw Ave.  
2017 Palmer Commons Bld.  
Ann Arbor, MI 48109-2218 USA  
Tel: 734-647-3113  
E-Mail: bjgrant@umich.edu

**Table S1. Analyzed crystallographic structures of G protein  $\alpha$  subunit.**

<b>PDB ID</b>	<b>Chain</b>	<b>Ligand</b>	<b>Source</b>	<b>Resolution</b>	<b>Reference</b>
<b>1FQJ</b>	A, D	ALF, GDP, MG	<i>Bos Taurus</i>	2	Slep et al. (2001)
<b>1FQK</b>	A, C	ALF, GDP, MG	<i>Bos Taurus</i>	2.3	Slep et al. (2001)
<b>1GOT</b>	A	MSE, GDP	<i>Bos Taurus</i>	2	Lambright et al. (1996)
<b>1TAD</b>	A, B, C	ALF, CA, CAC, GDP	<i>Bos Taurus</i>	1.7	Sondek et al. (1994)
<b>1TAG</b>	A	GDP, MG	<i>Bos Taurus</i>	1.8	Lambright et al. (1994)
<b>1TND</b>	A, B, C	CAC, GSP, MG	<i>Bos Taurus</i>	2.2	Noel et al. (1993)
<b>3V00</b>	A, B, C	GDP	<i>Bos Taurus</i>	2.9	Singh et al. (2012)
<b>1AGR</b>	A, D	ALF, CIT, GDP, MG	<i>Rattus Norvegicus</i>	2.8	Tesmer et al. (1997)
<b>1AS0</b>	A	GSP, MG, SO4	<i>Rattus Norvegicus</i>	2	Raw et al. (1997)
<b>1AS2</b>	A	GDP, PO4	<i>Rattus Norvegicus</i>	2.8	Raw et al. (1997)
<b>1BH2</b>	A	GSP, MG	<i>Rattus Norvegicus</i>	2.1	Posner et al. (1998)
<b>1CIP</b>	A	GNP, MG	<i>Rattus Norvegicus</i>	1.5	Coleman et al. (1999)
<b>1GFI</b>	A	ALF, GDP, MG	<i>Rattus Norvegicus</i>	2.2	Coleman et al. (1994)
<b>1GG2</b>	A	GDP	<i>Rattus Norvegicus</i>	2.4	Wall et al. Cell (1995)
<b>1GIA</b>	A	GSP, MG	<i>Rattus Norvegicus</i>	2	Coleman et al. (1994)
<b>1GIL</b>	A	GSP, MG	<i>Rattus Norvegicus</i>	2.3	Coleman et al. (1994)
<b>1GIT</b>	A	GDP, PO4	<i>Rattus Norvegicus</i>	2.6	Berghuis et al. (1996)
<b>1GP2</b>	A	GDP	<i>Rattus Norvegicus</i>	2.3	Wall et al. (1995)
<b>1KJY</b>	A, C	CS, GDP, MG	<i>Homo Sapiens</i>	2.7	Kimple et al. (2002)
<b>1SVK</b>	A	ALF, GDP, MG	<i>Rattus Norvegicus</i>	2	Thomas et al. (2004)
<b>1SVS</b>	A	GNP, MG	<i>Rattus Norvegicus</i>	1.5	Thomas et al. (2004)
<b>2GTP</b>	B	ALF, GDP, MG	<i>Homo Sapiens</i>	2.5	Soundararajan et al. (2008)
<b>2IHB</b>	A	ALF, GDP, MG	<i>Homo Sapiens</i>	2.7	Soundararajan et al. (2008)
<b>2ODE</b>	A, C	ALF, GDP, MG	<i>Homo Sapiens</i>	1.9	Soundararajan et al. (2008)
<b>2OM2</b>	A, C	GDP, MG	<i>Homo Sapiens</i>	2.2	Sammond et al. (2007)
<b>2V4Z</b>	A	ALF, GDP, MG	<i>Homo Sapiens</i>	2.8	Kimple et al. (2009)
<b>2XNS</b>	A, B	GDP, SRT,	<i>Homo Sapiens</i>	3.4	Sammond et al.



---

<b>2ZJY</b>	A	SO4 ALF, GDP, MG	<i>Rattus Norvegicus</i>	2.8	(2011) Morikawa et al. To be published
<b>3C7K</b>	C	ALF, GDP, MG	<i>Mus Musculus</i>	2.9	Slep et al. (2008)
<b>3FFA</b>	A	GSP, MG, SO4	<i>Rattus Norvegicus</i>	2.3	Kapoor et al. (2009)
<b>3ONW</b>	A, B	GDP, SO4	<i>Homo Sapiens</i>	2.4	Bosch et al. (2011)
<b>3QE0</b>	B	GDP, MG	<i>Homo Sapiens</i>	3	Bosch et al. (2012)
<b>3QI2</b>	A, B	GDP, GOL, SO4	<i>Homo Sapiens</i>	2.8	Bosch et al. (2012)
<b>4G5O</b>	A, D	CIT, GDP, SO4	<i>Homo Sapiens</i>	2.9	Jia et al. To be Published
<b>4G5Q</b>	A, D	GDP, SO4, CIT	<i>Homo Sapiens</i>	2.9	Jia et al. To be Published
<b>4G5R</b>	A	GDP, SO4, CIT	<i>Homo Sapiens</i>	3.5	Jia et al. To be Published

---

**Table S2. Normalized node degeneracy from path analysis of correlation networks derived from MD simulations.** For each network, 500 suboptimal paths were calculated. Nodes with degeneracy  $\geq 0.1$  in one or more networks are shown and corresponding degeneracy values are colored in red, green and blue, respectively, for GTP, GDP and GDI state networks. Source and sink nodes are highlighted in gray.

*Paths from  $\alpha 5$  to  $\gamma$ -Pi binding site*

SSE <sup>a</sup>	$\beta 1$				PL		$\alpha 1$	SI	$\beta 2$	$\beta 3$			
Residue	K31	L32	L33	L34	K42	S43	T44	T177	T178	I180	R193	M194	F195
GTP	0.51	0.70	0.36	0.11	0.00	0.01	0.00	0.25	0.18	0.17	0.21	0.31	0.64
GDP	0.00	0.00	0.00	0.00	0.89	0.47	0.94	0.00	0.00	0.00	0.00	0.00	0.00
GDI	0.00	0.00	0.00	0.00	0.02	0.70	0.99	0.00	0.00	0.00	0.00	0.00	0.00
Entropy <sup>b</sup>	0.66	0.89	0.90	0.84	0.83	0.85	0.86	0.82	0.48	0.80	0.42	0.81	0.55
SSE	SII			L10		$\alpha 5$							
Residue	D196	V197	G198	T323	D324	Q326	N327	V328	K329	F330	V331	F332	D333
GTP	0.58	0.54	1.00	0.00	0.00	0.00	0.00	0.00	0.00	0.00	0.00	0.00	0.00
GDP	0.09	0.07	1.00	0.91	0.95	0.39	0.69	0.10	0.57	0.37	0.23	0.67	0.22
GDI	0.85	0.94	1.00	0.95	0.83	0.31	0.78	0.05	0.17	0.52	0.44	0.50	0.17
Entropy	0.79	0.70	0.83	0.55	0.70	0.25	0.35	0.64	0.25	0.11	0.52	0.56	0.18
SSE	$\alpha 5$												
Residue	A334	V335	T336	D337	I338	I339							
GTP	0.00	0.00	0.00	0.00	0.00	1.00							
GDP	0.05	0.49	0.67	0.15	0.52	1.00							
GDI	0.20	0.34	0.60	0.05	0.15	1.00							
Entropy	0.18	0.69	0.24	0.49	0.34	0.74							

*Paths from  $\beta 1$  to RasD-HD interface*

SSE	$\beta 1$				PL		$\alpha 1$	LE			$\alpha F$		
Residue	K31	L32	L33	L34	K42	S43	T44	K47	N145	D146	S147	L171	R172
GTP	1.00	0.37	0.31	0.06	0.02	0.19	0.00	0.00	0.00	1.00	0.00	0.00	0.02
GDP	1.00	0.38	0.40	0.44	0.43	0.86	0.33	0.15	0.04	1.00	0.67	0.16	0.63
GDI	1.00	0.10	0.14	0.11	0.00	0.00	0.00	0.00	1.00	1.00	0.00	0.00	0.00
Entropy	0.66	0.89	0.90	0.84	0.83	0.85	0.86	0.80	0.07	0.83	0.27	0.82	0.48
SSE	SI						$\beta 2$			$\beta 3$			
Residue	S173	R174	V175	K176	T177	T178	G179	I180	I181	E182	T183	Q184	N191
GTP	0.00	1.00	0.67	0.57	0.69	0.16	0.00	0.06	0.00	0.00	0.00	0.00	0.00
GDP	0.65	0.85	0.01	0.00	0.00	0.00	0.00	0.00	0.00	0.02	0.02	0.00	0.01
GDI	0.00	1.00	0.81	0.57	1.00	0.68	0.65	0.51	0.39	0.36	0.31	0.18	0.16
Entropy	0.24	0.63	0.35	0.31	0.82	0.48	0.84	0.80	0.21	0.55	0.24	0.20	0.11
SSE	$\beta 3$				SII								

Residue	F192	R193	M194	F195	D196	V197	G198
GTP	0.00	0.25	0.33	0.68	0.68	0.44	0.10
GDP	0.08	0.34	0.29	0.40	0.46	0.01	0.00
GDI	0.46	0.59	0.30	0.48	0.30	0.35	0.13
Entropy	0.61	0.42	0.81	0.55	0.79	0.70	0.83

*Paths from  $\alpha 5$  to RasD-HD interface*

SSE	$\beta 5$	LG	$\alpha G$	L10	$\alpha 5$								
Residue	N265	K266	K267	T320	C321	Q326	N327	V328	K329	F330	V331	F332	D333
GTP	0.11	1.00	0.13	0.34	0.63	0.03	0.96	0.21	0.36	0.40	0.49	0.41	0.50
GDP	0.12	1.00	0.19	0.53	0.46	0.10	0.85	0.23	0.46	0.33	0.31	0.65	0.20
GDI	0.19	1.00	0.06	0.26	0.74	0.08	0.95	0.10	0.18	0.48	0.46	0.48	0.21
Entropy	0.78	0.94	0.14	0.60	0.31	0.25	0.35	0.64	0.25	0.11	0.52	0.56	0.18

SSE	$\alpha 5$					
Residue	A334	V335	T336	D337	I338	I339
GTP	0.36	0.19	0.37	0.38	0.79	1.00
GDP	0.06	0.50	0.65	0.18	0.56	1.00
GDI	0.24	0.39	0.52	0.14	0.24	1.00
Entropy	0.18	0.69	0.24	0.49	0.34	0.74

<sup>a</sup>SSE, secondary structure element.

<sup>b</sup>Entropy, sequence conservation (similar to the definition in (1)) derived from PFAM (2) “seed” alignment with accession number PF00503. Entries  $\geq 0.7$  are designated as highly conserved and are highlighted in yellow.

### Supplemental References

1. Grant, B. J., McCammon, J. A., Caves, L. S. D., and Cross, R. A. (2007) Multivariate analysis of conserved sequence-structure relationships in kinesins: coupling of the active site and a tubulin-binding sub-domain. *J Mol Biol* **368**, 1231-1248
2. Finn, R. D., Bateman, A., Clements, J., Coghill, P., Eberhardt, R. Y., Eddy, S. R., Heger, A., Hetherington, K., Holm, L., Mistry, J., Sonnhammer, E. L. L., Tate, J., and Punta, M. (2014) Pfam: The protein families database. *Nucleic Acids Res* **42**, D222-D230



## Dynamic Coupling and Allosteric Networks in the $\alpha$ Subunit of Heterotrimeric G Proteins

Xin-Qiu Yao, Rabia U. Malik, Nicholas W. Griggs, Lars Skjærven, John R. Traynor, Sivaram Sivaramakrishnan and Barry J. Grant

*J. Biol. Chem.* 2016, 291:4742-4753.

doi: 10.1074/jbc.M115.702605 originally published online December 24, 2015

---

Access the most updated version of this article at doi: [10.1074/jbc.M115.702605](https://doi.org/10.1074/jbc.M115.702605)

### Alerts:

- [When this article is cited](#)
- [When a correction for this article is posted](#)

[Click here](#) to choose from all of JBC's e-mail alerts

### Supplemental material:

<http://www.jbc.org/content/suppl/2015/12/24/M115.702605.DC1>

This article cites 53 references, 19 of which can be accessed free at <http://www.jbc.org/content/291/9/4742.full.html#ref-list-1>